

## SPECIAL REVIEW LECTURE

# Quantum Level Structures and Nonlinear Classical Dynamics

M. S. Child

*Physical and Theoretical Chemistry Laboratory, South Parks Road, Oxford OX3 1QZ, United Kingdom*

E-mail: [mark.child@chem.ox.ac.uk](mailto:mark.child@chem.ox.ac.uk)

Received July 2, 2001; in revised form September 6, 2001

The classical structure underlying the quantum mechanics of molecular vibrations is illustrated by reference to changes in vibrational energy distributions induced by increased anharmonic coupling as the energy increases. Specific applications to Fermi resonance models and to the level structures arising from cylindrically symmetrical saddle points are used to illustrate the relevance of classical bifurcation analysis, catastrophe theory, and quantum monodromy. © 2001 Elsevier Science

### I. INTRODUCTION

Now that it is possible to measure (1, 2) or calculate (1, 3, 4) hundreds of highly excited molecular vibrational states for a given system, far from the normal mode regime, there is a clear need for some interpretive structure. Fortunately there are many cases in which the eigenvalues fall into polyads (1, 2, 5–7), but there can also be subdivisions within a polyad. For example, the local mode polyads of H<sub>2</sub>O divide into an upper energy region where the eigenvalues are roughly equally spaced and a lower energy one containing close-lying local mode doublets (8, 9). It is difficult to specify such divisions objectively, by purely quantum mechanical techniques, except by plotting wavefunctions (1, 4), because the eigenvectors in any convenient basis are too heavily mixed to allow easy assignment. The purpose of this paper is to offer an alternative interpretive approach, via the correspondence with classical mechanics (10), which has a more sharply defined analytical structure than quantum mechanics. There are of course well-known connections between the shapes of classical trajectories and those of the corresponding wavefunctions (1, 7, 8), but these are not amenable to experimental verification. Our prime focus is on the classical origin of observable changes in the vibrational eigenvalue distributions.

Returning to the relatively familiar local mode context (11), the above division of the eigenvalues into “normal” (roughly equally spaced) and “local” (doubled eigenvalue) groups is associated with a bifurcation of the classical phase space into two parts, one occupied by “normal trajectories,” with the same symmetry as the potential energy function, and the other by two or more classically degenerate “local mode” trajectories oscillating around the directions of the individual bonds in the molecule. The point of the paper is that this is not an isolated phenomenon, and Section 2 below illustrates, behavior qualitatively similar be-

havior, with a richer topology, at a Fermi resonance—similar in the sense that each bifurcation of the classical phase space is accompanied by a corresponding bifurcation of the quantum eigenvalue spectrum. Such changes are easy to recognize in systems involving a single resonance, but the effect is quite general—as illustrated by a recent study of the relatively complex bending vibrational dynamics of acetylene (5). The main purpose of Section 2 is to demonstrate the practical significance of important papers by Li, Xiao, and Kellman (6, 7).

A second interesting complication of the vibrational dynamics arises from the presence of a saddle point on the potential surface, such as the barrier to linearity in H<sub>2</sub>O or to internal rotation in HCP. There is a considerable literature from the 1960's on bent to linear vibrational structures—see in particular Dixon (12) and Johns (13)—but the generality of the vibrational structures associated with systems having cylindrically symmetric potential barriers has only recently been recognized under the term ‘quantum monodromy’ (14). Again the quantum eigenvalue structures can be directly related to abrupt changes in the classical dynamics, and the associated theory is outlined in Section 3. Finally, Section 4 of the paper summarizes the main conclusions.

### II. FERMI RESONANCE DYNAMICS

The influence of classical phase space bifurcations on quantum eigenvalue distributions is conveniently demonstrated by reference to the standard Fermi resonance Hamiltonian

$$H = \omega_1 \left( v_1 + \frac{1}{2} \right) + \omega_2 \left( v_2 + \frac{1}{2} \right) + \sum_{i < j} x_{ij} \left( v_i + \frac{1}{2} \right) \times \left( v_j + \frac{1}{2} \right) + k_{122} (\hat{a}_1^\dagger \hat{a}_2^2 + \hat{a}_1 \hat{a}_2^{\dagger 2}). \quad [1]$$

It is assumed that  $\omega_1 \simeq 2\omega_2$  and that  $x_{ij}$  and  $k_{122}$  are small compared with the  $\omega_i$ . Conservation of the polyad quantum number

$$n_p = 2v_1 + v_2 \quad [2]$$

means that interest can be focussed on the classical origin of changes in the intra-polyad eigenvalue splittings from one polyad to the next.

Equation [1] has a valuable role for the fitting and interpretation of observed spectra (*I, 15*), but our quite different aim is to demonstrate the existence of quite sharp changes in the vibrational eigenvalue distributions, that are intimately related to changes in the underlying classical dynamics. The following sections illustrate the significance of a so-called classical bifurcation (*16*) by reference to classical trajectory plots, Poincaré surfaces of sections, and changes in the nature of classical periodic orbits. Further extensions, due to Li, Xiao, and Kellman (*6, 7*), use the techniques of catastrophe theory (*17*) to provide an generic overview of the influence of the parameter choices in Eq. [1] on the eigenvalue distribution of any 2 : 1 Fermi resonant system.

### II.1. Classical Phase Space Bifurcations and Quantum Eigenvalue Patterns

A classical equivalent of the Hamiltonian in Eq. [1] may be obtained by the substitutions

$$v_i + \frac{1}{2} = \frac{1}{2}(p_i^2 + q_i^2), \quad [3]$$

$$\hat{a}_i = \frac{1}{\sqrt{2}}(q_i - ip_i), \quad \hat{a}_i^\dagger = \frac{1}{\sqrt{2}}(q_i + ip_i), \quad [4]$$

so that

$$\hat{a}_1^\dagger \hat{a}_2^2 + \hat{a}_1 \hat{a}_2^{\dagger 2} = \frac{1}{\sqrt{2}}[q_1(q_2^2 - p_2^2) + 2p_1 p_2 q_2]. \quad [5]$$

It is also convenient for presentational purposes to introduce new variables

$$(x, p_x) = (q_1, p_1), \quad (y, p_y) = (\gamma q_2, p_2/\gamma), \quad [6]$$

where  $\gamma = \sqrt{\omega_1/\omega_2}$ , in order to give the kinetic energy a common coefficient of  $p_x^2$  and  $p_y^2$ , in which case the classical trajectories may be visualized as a ball rolling in  $(x, y)$  space. The so-called canonical nature (*18*) of the  $(y, p_y)$  scaling in Eq. [6] ensures that Hamilton's equations (*18*) apply in the  $(x, p_x, y, p_y)$  system.

Three classical trajectories of the resulting Hamiltonian are shown in the upper panels of Fig. 1, using parameter values derived from the spectrum of  $\text{CHCl}_3$  (*19*). The outer boundaries

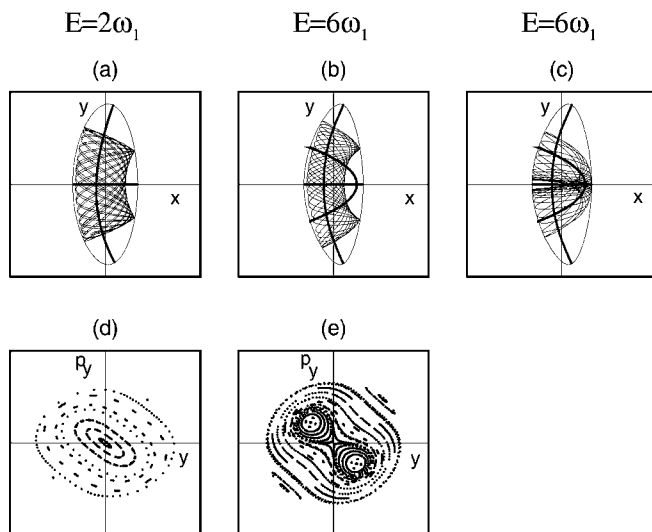


FIG. 1. (a)–(c) Classical trajectories and (d), (e) Poincaré sections for the Fermi resonance model in  $\text{CHCl}_3$  (*19*). The outer boundaries in the upper plots are potential energy contours. Heavy solid lines are classical periodic orbits. The netlike figures are individual trajectories. Separate rings of dots in the lower Poincaré section were each generated by different trajectories.

in Figs. 1a–1c indicate the potential energy contours, the netlike patterns are individual classical trajectories, and the heavy solid lines are simple periodic orbits of the motion, which run indefinitely to and fro along the same path. The first point to notice is that Fig. 1a, at  $E = 2\omega_1$ , shows just two simple periodic orbits, whereas the higher energy plots in Figs. 1b and 1c contain three. Second, the shape of the trajectory in Fig. 1a is dictated by the shapes of the two periodic orbits, in the sense that the caustic corners, at which the trajectory touches the potential contour, lie in the four quadrants between these orbits. The trajectory in Fig. 1b is similar in shape, whereas the one in Fig. 1c is clearly guided by the new horse-shoe shaped or “Fermi resonance” periodic orbit.

The appearance of new periodic orbits, resulting in the coexistence of different trajectory types at a given energy, is the signature of a classical bifurcation (*16*). Another view is provided by the Poincaré sections in Figs. 1d and 1e, which are constructed by plotting values of  $y$  and  $p_y$  whenever the trajectory crosses a given line  $x = \text{const}$  with  $p_x > 0$ . The central point in each diagram is the Poincaré image of the horizontal, symmetry-determined, periodic orbit in Figs. 1a–1c, which necessarily cuts any line  $x = \text{const}$  with  $y = p_y = 0$ . The seven rings around this central point in Fig. 1d are Poincaré maps of seven different trajectories, all broadly similar in shape to the one in Fig. 1a. The pattern in Fig. 1e is quite different, because the map is now divided into two regions—an outer one occupied by trajectories of the form in Fig. 1b and an inner one occupied by those similar to the one in Fig. 1c. The origin of this important difference is that the symmetry-determined periodic orbit has changed its character between  $E = 2\omega_1$  and  $E = 6\omega_1$ . It is stable to small perturbations in Fig. 1a, causing neighboring

trajectory intersections to circle around it in Fig. 1d, but it has become unstable at  $E = 6\omega_1$ , causing neighboring points to move away from the center of Fig. 1e.

Interested readers may wish to refer to the known quantization procedures (10, 20) for relating the energies of particular classical trajectories to the quantum mechanical eigenvalues. In addition the well-known influence of periodic orbits in guiding the shapes of Fermiresonant wavefunctions (7) may be noted. There is also a considerable literature (21–23) on periodic orbit related wavefunctions of classically chaotic systems. It is, however, sufficient for the present discussion of eigenvalue patterns to note that stable and unstable periodic orbits act in effect as potential wells and potential barriers to motions transverse to the periodic orbit motion. The quantum level separations associated with (narrow) trajectories close to a stable orbit will therefore be governed by the classical frequency of this transverse motion; and one can expect a “Dixon dip” (12) in the level separations associated with trajectories close to an unstable periodic orbit (24).

These qualitative expectations are precisely fulfilled by the change in polyad splitting patterns shown for the  $\text{CHCl}_3$  model (19) in Fig. 2 (25). The eigenstates are conveniently labeled by the polyad quantum number  $n_p$ , given by Eq. [2], and a counting number  $n$  along the polyad. For ease of comparison with other systems, Fig. 2 shows the  $n_p$  dependence of the polyad splitting

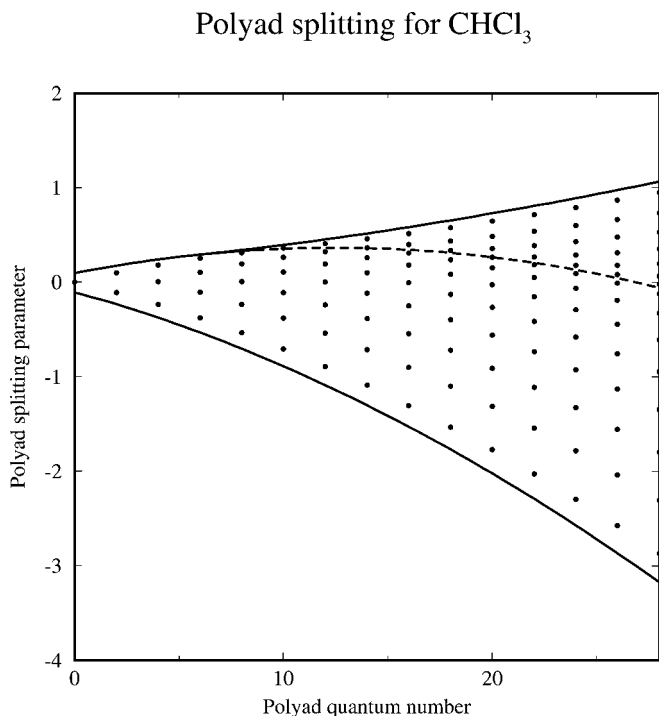


FIG. 2. The polyad splitting pattern for the Fermi resonance model of  $\text{CHCl}_3$ . Heavy solid lines are the energies of quantized stable classical periodic orbits, with actions equivalent to the polyad quantum number. The dashed line is the corresponding energy of the unstable periodic orbit associated with the central pattern in Fig 1e.

parameter

$$\Delta(n, n_p) = [E(n, n_p) - E^0(n_p)]/\omega_1, \quad [7]$$

where

$$E^0(n_p) = \frac{1}{4}(\omega_1 + 2\omega_2)\left(n_p + \frac{3}{2}\right) + \frac{1}{16}(x_{11} + 2x_{12} + 4x_{22})\left(n_p + \frac{3}{2}\right)^2. \quad [8]$$

A bifurcation of the quantum eigenvalue distribution at  $n_p \simeq 10$  is clearly apparent from the sudden onset of a set of relatively closely spaced higher energy eigenvalues in each polyad. The underlying classical origin is indicated by the heavy continuous and dashed lines, which show the reduced energies of the stable and unstable periodic orbits with classical actions  $\frac{1}{2\pi} \int \mathbf{p} \cdot d\mathbf{q}$  equal to  $(n_p + 1)h$ . The closely spaced upper eigenvalues in each polyad are associated with horseshoe-shaped trajectories like the one in Fig. 1c, whose Poincaré images lie inside the “resonance zone” in Fig. 1e, while the more widely spaced energy levels belong to trajectories like the one in Fig. 1d, which lies outside the resonance zone. It should also be noted that the lower continuous curve lies systematically below the energy of the lowest eigenvalue, by an amount roughly equal to half the local eigenvalue separation, because the energy of the quantized periodic orbit must be corrected for the zero-point energy of the transverse vibrational motion. A similar correction also applies at the high energy end of each polyad, except that the zero-point energy is subtracted from the energy of the quantized periodic orbit. The reason for this difference is discussed below.

## II.2. The Fermi Resonance Catastrophe Map

Xiao and Kellman (7) have taken the classical discussion further by transforming the classical Hamiltonian to angle-action variables (10, 18) and exploiting the conservation of  $n_p$ . In outline, the angle-action transformation takes the form

$$v_i + \frac{1}{2} = I_i, \quad [9]$$

$$\hat{a}_i = \sqrt{I_i}e^{-i\phi_i}, \quad \hat{a}_i^\dagger = \sqrt{I_i}e^{i\phi_i}, \quad [10]$$

where  $\phi_i$  is the angle variable conjugate to the action  $I_i$ . Further transformations

$$I_1 = I + J, \quad I_2 = 2(I - J), \quad [11]$$

$$\theta = \phi_1 + 2\phi_2, \quad \psi = \phi_1 - 2\phi_2 \quad [12]$$

cast the Hamiltonian into the form

$$H = H^0(I) + H'(J, \psi; I), \quad [13]$$

where

$$H^0(I) = (\omega_1 + 2\omega_2)I + (x_{11} + 2x_{12} + 4x_{22})I^2 \quad [14]$$

and

$$H'(J, \psi; I) = 2\gamma_2 I^2 \left[ \beta \left( \frac{J}{I} \right) + \frac{1}{2} \left( \frac{J}{I} \right)^2 + \mu \left( 1 + \frac{J}{I} \right)^{1/2} \left( 1 - \frac{J}{I} \right) \cos \psi \right]. \quad [15]$$

Other notations are

$$\beta = \frac{\omega_1 - 2\omega_2 + 2(x_{11} - 4x_{22})I}{2\gamma_2 I}, \quad [16]$$

$$\mu = \frac{k_{122}}{2\gamma_2 \sqrt{I}}, \quad [17]$$

and

$$\gamma_2 = x_{11} + 4x_{22} - 2x_{12}. \quad [18]$$

The important points to note are as follows:

- The angles  $\theta$  and  $\psi$  are conjugate to  $I$  and  $J$ , respectively.
- $H$  is independent of  $\theta$ , which means that  $I$ , which actually equals  $n_p/4$ , is a constant of the motion. The advantage for the classical theory is that the transformation to  $(I, \theta, J, \psi)$  reduces the number of active degrees of freedom from 4 to 2. In particular the determination of classical periodic orbits reduces to finding fixed points of  $H'(J, \psi; I)$ , at which

$$\frac{\partial H'}{\partial J} = \frac{\partial H'}{\partial \psi} = 0. \quad [19]$$

- The stability of a given fixed point depends on the Hessian determinant,  $\det h$ , of the matrix of second derivatives of  $H'(J, \psi; I)$ ; the corresponding periodic orbit is stable or unstable according to whether  $\det h$  is positive or negative (16). Moreover the zero-point energies for motions transverse to stable periodic orbits are given by  $\pm \frac{\hbar}{2} \sqrt{\det h}$ , where the sign depends on whether the eigenvalues of the Hessian matrix  $h$  are both positive or both negative (9) (their product is of course equal to  $\det h$  which is positive at the stable points). These considerations explain why the eigenvalues, represented by points in Fig. 2, lie between the energies of the quantized periodic orbits, represented by continuous lines.

- The organization of the roots of Eq. [19] depend on two parameters  $\beta$ , which is a measure of the detuning of the system and  $\mu$ , which is a scaled coupling strength. Consequently the bifurcation behavior of all Fermi resonant systems can be displayed in the two parameter  $(\beta, \mu)$  plane. Moreover the  $I$

dependence of  $\beta$  and  $\mu$  means that changes from one polyad to another for a given system lie on a parabola in this plane.

Xiao and Kellman (7) provide interesting geometrical insight by substituting  $J/I = \cos \alpha$ , which casts the motion onto the surface of a “polyad sphere” with spherical polar angles  $\alpha$  and  $\psi$ . Space precludes following the details here, but the upshot is that two types of stationary point are found. The first, which lies at the north pole,  $\alpha = 0$ , where  $I = J$ , corresponds to the symmetry determined horizontal stretching orbit in Figs. 1a–1c, because Eq. [11] shows that the bending action  $I_2 = 0$  at this point. It is found to change from stable to unstable on the lines

$$\beta + 1 \pm 2\sqrt{2}\mu = 0 \quad [20]$$

in the  $(\beta, \mu)$  plane, and a new stable fixed point appears, corresponding to the horseshoe orbit in Fig. 1c. The second type of stationary point lies at  $\psi = 0$  or  $\pi$ , with  $\alpha$  given by a cubic expression in  $\cos \alpha/2$ . Two situations apply, since the real cubic equation can have either one or three real roots. One of these fixed points, which corresponds to the near vertical bent orbit in Figs. 1a and 1b, is always found to be stable. The second pair, one of which is stable and the other unstable, appear at a so-called “saddle node” bifurcation (16), on particular lines in the  $(\beta, \mu)$  plane;

- The complete bifurcation diagram shown in Fig. 3 is sometimes called a “catastrophe map” because the topology of the coalescence stationary points of algebraic polynomials is the realm of catastrophe theory (17). Our present use of this diagram is to predict and interpret changing patterns in the eigenvalue distributions of Fermi resonant systems, by following the paths traced out as the polyad quantum number increases. For example the filled circles marked  $\text{CHCl}_3$  correspond to successive polyads shown in Fig. 2. The path starts in region I, where there are two fixed points of  $H'(J, \psi; I)$ , corresponding to the two stable periodic orbits in Fig. 1a and passage into region II leads to instability at the north pole and the birth of a new fixed point, corresponding to the horseshoe periodic orbit in Fig. 1c. The associated bifurcation of the polyad splitting pattern in Fig. 2 has already been discussed.

A second example of such polyad splittings is provided by a parameter fit to the  $\text{CHD}_3$  spectrum (26), except that the sign of  $\mu$  has been reversed for illustrative purposes in Fig. 3. The path in the  $(\beta, \mu)$  plane again starts in region I but now passes through regions II and III to reach region IV. Corresponding changes in the polyad splitting pattern are shown in Fig. 4, where (as in Fig. 2) solid and dashed lines show the energies of stable and unstable periodic orbits as a function of their classical actions. Vertical lines mark the passage from one region of Fig. 3 (25) to the next. Again it is clear that the energies of the quantized periodic orbits are intimately connected with changes in the polyad eigenvalue splitting patterns. Thus the passage from region I to

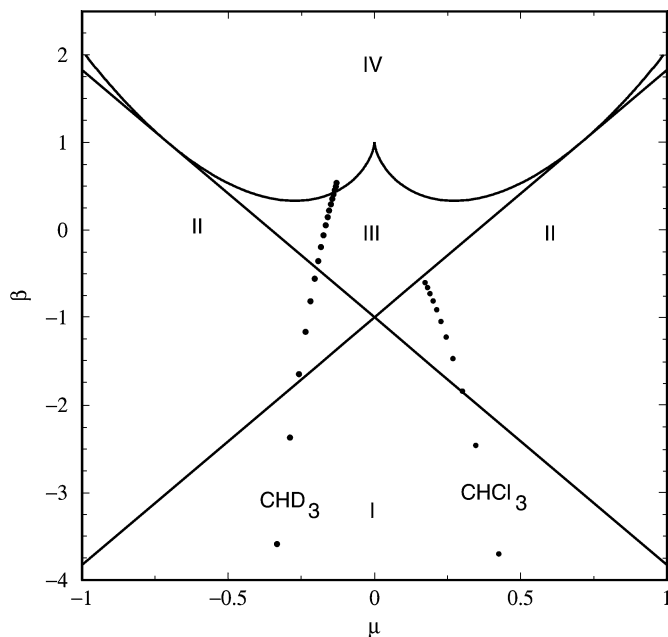


FIG. 3. The Xiao-Kellman catastrophe map for the Hamiltonian in Eq. [1]. The axis labels  $\mu$  and  $\beta$  are the combinations of parameters given by equations [16] and [17]. Dots signify  $(\mu, \beta)$  combinations for successive polyads of model  $\text{CHCl}_3$  to the right and  $\text{CHD}_3$  to the left. The lines signify bifurcations on passing from region to another, with the fixed points in different regions being specified as follows: I (two stable), II (two stable, one unstable), III (three stable, one unstable), IV (two stable).

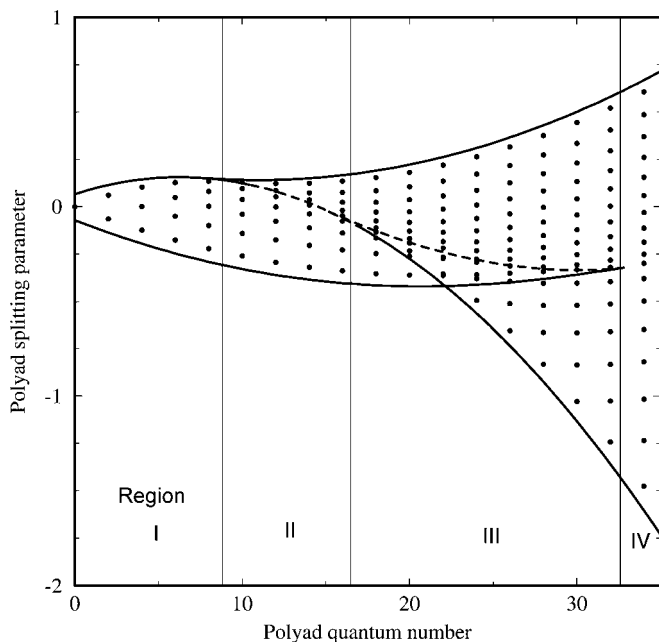


FIG. 4. The polyad splitting pattern for the Fermi resonance model of  $\text{CHD}_3$ . Heavy solid lines are the energies of quantized stable classical periodic orbits, with actions equivalent to the polyad quantum number. Regions I-IV are the regions in Fig. 3.

region II is accompanied by a division of the eigenvalue splitting pattern similar to that in Fig. 2. The transition to region III sees the north pole (pure stretching orbit) revert to stability, with the birth of a new unstable orbit. Finally this new orbit annihilates with what is predominantly a pure bending orbit at a reverse saddle node bifurcation at the boundary between regions III and IV.

### III. BENT-TO-LINEAR LEVEL STRUCTURES AND QUANTUM MONODROMY

New insights into generic eigenvalue distributions at cylindrically symmetric quadratic maxima have been collected under the term “quantum monodromy” (14). The prototype is the two-dimensional champagne bottle model (27), with the Hamiltonian

$$H = -\frac{\hbar^2}{2m} \left\{ \frac{1}{r} \frac{\partial}{\partial r} \left( r \frac{\partial}{\partial r} \right) - \frac{1}{r^2} \frac{\partial^2}{\partial \phi^2} \right\} - ar^2 + br^4. \quad [21]$$

Models of this type were widely studied in the 1960's in the context of bent-to-linear transitions in molecules such as  $\text{H}_2\text{O}$ . Johns (13), for example, established the connection between the bent and linear molecule quantum numbers,  $|v_2^{\text{bent}} K\rangle$  and  $|v_2^{\text{linear}} l\rangle$ ; but it is less often realized that the algebraic relations  $l = K$  and  $v_2^{\text{linear}} = 2v_2^{\text{bent}} + l$  between the two sets imply that both designations are equally valid for any particular energy state. In addition Dixon (12) drew attention to the presence of a sharp dip in the local  $K = 0$  vibrational energy spacing at the barrier to linearity, which is smoothed away as  $K$  increases. It has only recently become apparent, however, that Dixon's observations imply a form of dislocation in the quantum eigenvalue distribution that is generic to all systems with a cylindrically symmetric barrier—a phenomenon known as “quantum monodromy.”

Figure 5 illustrates a typical quantum eigenvalue lattice for the champagne bottle in  $(k, E)$  space, where  $k$  is the signed value of  $K$ . Solid lines join points with common bent vibrational labels  $v_2^{\text{bent}}$  and dashed lines those with common values of  $v_2^{\text{linear}}$ . The generic feature is that the smooth roughly quadratic curves showing the rotational energy dependence of low-lying  $v_2^{\text{bent}}$  states go over abruptly to sharply kinked curves at energies above the barrier. Similarly the smooth dashed curves in the upper part of the diagram go over to kinked ones at energies below the barrier.

The classical interpretation of this characteristic energy level pattern relies on interpreting the solid curves in Fig. 5 as contours of a continuous classical energy function, or Hamiltonian,  $\tilde{H}[(v_2^{\text{bent}} + \frac{1}{2})\hbar, k\hbar]$ , at given values of  $v_2^{\text{bent}}$ . We write  $\tilde{H}$  rather than  $H$  because  $\tilde{H}[(v_2^{\text{bent}} + \frac{1}{2})\hbar, k\hbar]$  is the angle-action transform of the Hamiltonian in Eq. [21], dependent, via the correspondence principle (10), only on the actions

$$I_r = \left( v_2^{\text{bent}} + \frac{1}{2} \right) \hbar \quad \text{and} \quad I_\phi = k\hbar. \quad [22]$$

## champagne bottle

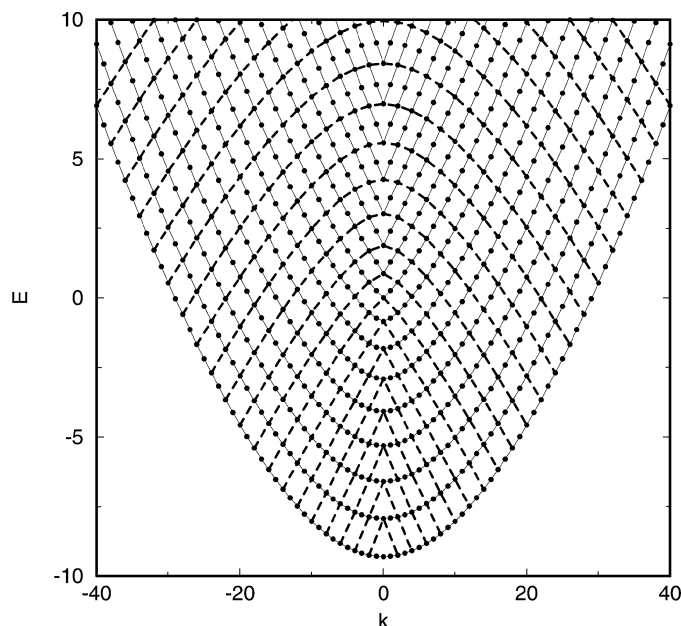


FIG. 5. Quantum states of the champagne bottle Hamiltonian, organized by the signed angular momentum,  $k$ , and the energy,  $E$ . Solid and dashed lines join points of constant  $v_2^{\text{bent}}$  and  $v_2^{\text{linear}} = 2v_2^{\text{bent}} + |k|$  respectively. Note, in the limit  $k \rightarrow 0$ , that the solid lines have zero derivative with respect to  $k$  at  $E < 0$  but become sharply kinked for  $E > 0$ , while the opposite is true for the dashed lines.

It follows that the slopes of the solid lines in Fig. 5 are related to the precessional rates of the classical trajectories, because according to Hamilton's equations (18)

$$\omega_\phi = \frac{d\phi}{dt} = \left( \frac{\partial \tilde{H}}{\partial I_\phi} \right)_{v_2^{\text{bent}}} = \frac{1}{\hbar} \left( \frac{\partial \tilde{H}}{\partial k} \right)_{v_2^{\text{bent}}}. \quad [23]$$

Now both the angular and radial frequencies,  $\omega_\phi$  and  $\omega_r$ , are constants for any trajectory, so that  $\omega_\phi$  may be evaluated as  $\omega_\phi = \omega_r(\Delta\phi/2\pi)$ , where  $\Delta\phi$  is the angular change over one cycle of the radial motion. In other words, the slopes of solid lines in Fig. 1 may be expressed as

$$\left( \frac{\partial \tilde{H}}{\partial k} \right)_{v_2^{\text{bent}}} = \frac{\hbar\omega_r}{2\pi} \Delta\phi, \quad [24]$$

which means that the discontinuous change in the limiting slope at  $k = 0$ , on crossing from  $E < 0$  to  $E > 0$ , may be associated with the discontinuous change in the nature of the associated classical trajectory shown in Fig. 6. The negative energy trajectory precesses in a counter-clockwise sense at a rate dependent on the angular momentum  $k$ ; thus it is easy to see that the angle change  $\Delta\phi$  over one vibrational period falls to zero in the limit  $k = 0$ . On the other hand positive energy trajectories with

positive and negative  $k$  pass above and below the central point respectively, and the trajectory over one cycle of the radial motion draws out a diameter of the bounding circle in the limit  $k \rightarrow 0$ ; hence the angle change  $\Delta\phi = \pm\pi$  for all positive-energy, zero-angular momentum trajectories, with the upper or lower sign taken for the limit  $k \rightarrow 0_+$  or  $k \rightarrow 0_-$ , respectively.

Notice that this classical interpretation focuses only on the presence of the cylindrically symmetric barrier. The shape of the potential function elsewhere affects the vibrational frequency, but it cannot induce additional precessional effects in the limit  $k = 0$ . Zero angular momentum trajectories at subbarrier energies will always be reflected back along their paths with  $\Delta\phi = 0$ , while those with energies above the barrier will experience limiting angle changes of  $\Delta\phi = \pm\pi$  as  $k \rightarrow 0_\pm$  during one cycle of the variable governing the shape of the barrier.

Figure 7 shows how knowledge of the generic behavior of such systems can be used to assist the assignment and interpretation of the computed  $(0\ v_2\ 0)$  vibrational states of  $\text{H}_2\text{O}$  (14). The computed data were taken from Partridge and Schwenke (3), using rotational energies of the  $J_{J_0}$  states; thus  $k_a = \pm J$ . Asymmetry splittings between different  $K_c$  components are negligibly small on the scale of the diagram. Despite possible coupling to the stretching vibrational modes, the characteristic monodromic pattern is clearly apparent in Fig. 7. It is therefore evident, from the location of the first kinked curve, that the energy of the barrier to linearity lies at roughly  $11\ 000\ \text{cm}^{-1}$ , after correction for zero-point vibrational motion. Moreover the existence of the double grid, with lines of constant  $v_2^{\text{bent}}$  (solid) and  $v_2^{\text{linear}}$  (dashed), allows confident reassignment with respect to  $v_2$  of points with superimposed crosses. Similar plots are reported elsewhere (14) for bending progressions with other states of excitation in the stretching modes.

Figure 8 confirms that the same qualitative abrupt reorganization of the eigenvalue pattern for the spherical pendulum model

$$H = \frac{1}{2I} J^2 + B \cos \theta, \quad [25]$$

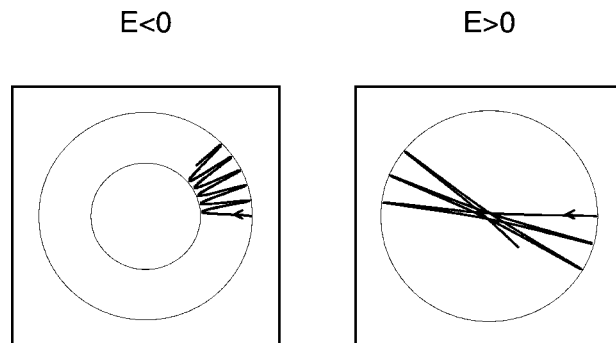


FIG. 6. Classical trajectories for the champagne bottle Hamiltonian, drawn for positive angular momentum,  $k$ . Note that the angular change  $\Delta\phi$  over one cycle of the radial motion tends to zero as  $k \rightarrow 0$  at negative energies, but to  $\pi$  at positive energies.

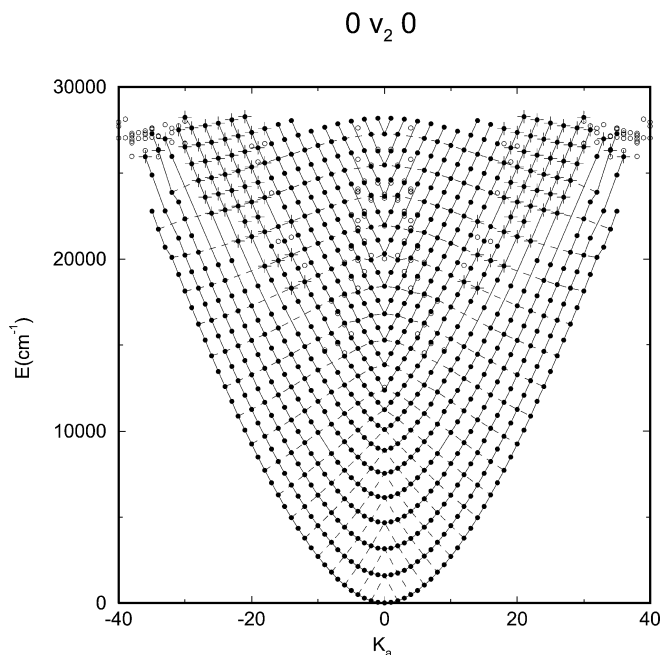


FIG. 7. Quantum monodromy plot of the bending ( $0v_20$ ) progression of  $H_2O$  taken from the data of Partridge and Schwenke (3). Rotational energies are for  $J_0$ ; hence  $k_a = \pm J$ . The solid circles, which are joined by solid and dashed lines, display the monodromic pattern illustrated in Fig. 5. Those with superimposed crosses have been reassigned with respect to  $v_2$ , keeping  $k$  constant.

### spherical pendulum

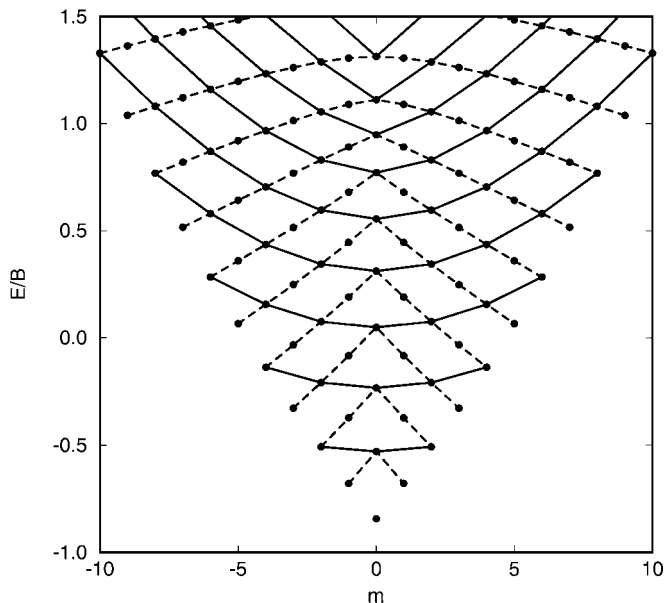


FIG. 8. Quantum monodromy in the spectrum of the spherical pendulum Hamiltonian. Points are labeled upward from zero in each column by a quantum number  $v_\theta$ . Solid lines join those with common  $v^{\text{linear}} = 2v_\theta + |m|$ , while the dashed lines join those with common  $j = v_\theta + |m|$ .

which is applicable to the pendular states of dipolar species in strong electric fields and to the bending/rotational motions of HCP (28, 29). The magnetic quantum number is now denoted by  $m$  and solid curves join points with common values of the degenerate oscillator quantum number, analogous to the previous  $v^{\text{linear}}$ . The dashed curves are labelled by common values of the total angular momentum quantum number  $j = v^{\text{linear}} - |m|$ . The relevance of this diagram to drastic changes in the spectroscopic rotational-vibrational parameters of HCP, as signatures of bond-breaking internal rotation, are discussed elsewhere (28).

Finally a word about the origin of the term “quantum monodromy.” As shown elsewhere (14), the presence of an apparent dislocation in the lattices of quantum eigenvalues shown in Figs. 5–7 causes any unit cell of the lattice to change its shape if it is smoothly transported around the critical point at the energy of the barrier maximum. The term monodromy, meaning *once round*, comes from the classical mechanical literature (30, 31), where corresponding changes in the classical action lattice are seen as topological obstructions to construction of a smooth system of angle-action variables. A closely related aspect, which unifies the quantum and classical pictures, is that the Bohr–Sommerfeld quantization integral (10)

$$v_2^{\text{bent}}(k, E) + \frac{1}{2} = \frac{1}{h} \oint p(E, k; r) dr \quad [26]$$

is a nonanalytic function of  $k$  and  $E$ , with a logarithmic branch point at  $k = E = 0$  (14). Distortion of the unit cell during transport of a unit cell of the quantum lattice around the critical central point may therefore be attributed to passage from one Riemann sheet (32) to another, at a branch cut emanating from the critical point. These mathematical details are perhaps irrelevant in a typical spectroscopic context, but it is desirable to have a term to emphasize the generic aspect of the above eigenvalue reorganizations, and “quantum monodromy” was coined to fit the bill.

## IV. DISCUSSION

The purpose of this article has been to illustrate how the distributions of quantum mechanical eigenvalues reflect underlying changes in the classical dynamics of the system. Attention was restricted to relatively simple systems, with two active degrees of freedom, but the aim was to demonstrate quite general phenomena. For example, the idea that a classical bifurcation divides the classical phase space into two or more parts, each with its own localized eigenvalue spectrum, is not limited to two degrees of freedom. Similar bifurcations must occur for all polyatomic species, as the energy increases towards the dissociation limit, although the situation may be further complicated by classically chaotic effects arising from the Chirikov (33, 34) overlap of different resonances. The reorganization of energy levels at a cylindrically symmetric barrier in two degrees of freedom is another type of gross change that seems, at least in the case of

H<sub>2</sub>O (14), to be relatively unaffected by the state of excitation in other modes.

The discussion of Fermi resonance dynamics in Section 2 was intended to provide an introduction to classical mechanical techniques and classical lines of thought. The illustrations were provided by parameter sets determined by the spectra of CHCl<sub>3</sub> (19) and CHD<sub>3</sub> (26), but the extrapolations to quite high polyad numbers should be taken to be illustrative rather than predictive, in view of the possible onset of other resonances as the energy increases. It is, however, worth emphasizing the richness of the Fermi resonance dynamics in allowing not only simple bifurcations analogous to the local mode bifurcations in symmetrical hydrides (11) but also “saddle node bifurcations” giving rise to the simultaneous appearance (or disappearance) of stable and unstable pairs of periodic orbits, the occurrence of which can give rise to more complicated energy level splitting patterns, such as that in Fig. 3. Such saddle node bifurcations have also been found in classical periodic orbit studies on realistic potential surfaces (1, 35). The beauty of the full model theory, due to Xiao and Kellman (7), is not only that their possible occurrence is embodied in the much simpler effective Hamiltonian model, but also that their onset can be predicted in terms of the magnitudes of the two parameter combinations  $\mu$  and  $\beta$  given by Eqs. [16] and [17].

The second part of the paper concerned so called “quantum monodromy” arising from reorganization of the quantum mechanical energy levels at a cylindrically symmetrical saddle point, such as the barrier to linearity in H<sub>2</sub>O (14) or the barrier to bond-breaking internal rotation in HCP (28), both of which involve a transition between two different types of motion—either bent to linear motion (13, 12) in H<sub>2</sub>O or vibrational to rotational motion in HCP (28). The purpose was to demonstrate, first that every eigenvalue of such systems can be labeled by two (or possibly more) sets of quantum numbers, one for each of the possible limiting types of motion, creating a double grid, which may be of considerable value for the assignment of highly excited quantum states. Moreover the resulting quantum lattice in energy and angular momentum space has a characteristic type of dislocation at the energy and angular momentum of the barrier, the observation of which immediately fixes the energy of the barrier. The nature of the vibrational reorganization also has clear implications for rapid increases in spectroscopic vibrational-rotational parameters as the energy rises towards the barrier maximum (28).

Since the illustrations above are limited to systems with two degrees of freedom, it is natural to consider whether similar considerations apply to higher dimensional systems. One important consideration is that the dimensionality of the nonlinear dynamics problem depends not on the absolute dimensionality of the system, but on the number of anharmonic resonances in the effective Hamiltonian (36). We have already seen for example that the two-dimensional Hamiltonian in Eq. [1] is reduced by the semiclassical transformation to the one-dimensional form in Eq. [15]. Much of the theory for interacting resonances remains

to be developed, but recent papers on interacting local mode and Fermi resonances in H<sub>2</sub>O (6, 37–41) may serve to indicate what can be done. In the first place the presence of two resonances in a three-dimensional system implies the existence of a conserved polyad number

$$P = v_1 + v_2 + \frac{1}{2}v_b, \quad [27]$$

where  $v_1$  and  $v_2$  are local stretching quantum numbers and  $v_b$  applies to the bend. Consequently classical Poincaré surfaces, such as those in Fig. 1, may be employed to analyze changes in the two-dimensional reduced classical dynamics as  $P$  increases. The primary periodic orbits, emanating from the normal modes, play little part in organizing the spectrum, except in the lowest polyads (39, 41), but subsequent bifurcations (38, 39) lead to Poincaré sections that show a clear division into local mode, normal mode, and Fermi resonance regions at  $P = 8$  (39), which spans the energy range 25 000–27 500 cm<sup>-1</sup>. Analysis of the wavefunctions confirms that all but 2 of the 47 states in this  $P = 8$  polyad fall into the above three categories. It should be noted, however, that the Fermi resonance is fairly weak at  $P = 8$ , as evidenced by the fact that the eigenvalues fall into only slightly perturbed local mode polyads (40). The situation is, however, complicated at  $P = 16$  due to the onset of widespread classical chaos. Nevertheless a combined phase space analysis of the wavefunctions and Poincaré surfaces can still be used to assign most of the individual eigenstates (41).

Turning to multi-dimensional aspects of the quantum monodromy, the qualitative eigenvalue pattern in Fig. 7 is known to persist for a variety of  $v_2$  progressions with different stretching quantum numbers (14). However, careful numerical investigations (1) and model calculations (28, 42, 43) for HCP indicate quite drastic changes to the classical and quantum dynamics on approaching a saddle point on the potential surface, and similar complications are anticipated close to and above the barrier to linearity in H<sub>2</sub>O. Further progress in the application of nonlinear dynamics awaits the development of an effective Hamiltonian model for the treatment of saddle point effects.

## ACKNOWLEDGMENT

The author acknowledges the assistance of C. D. Cooper in helpful discussions and invaluable assistance in drawing the diagrams.

## REFERENCES

1. H. Ishikawa, R. W. Field, S. C. Farantos, M. Joyeux, J. Koput, C. Beck, and R. Schinke, *Annu. Rev. Phys. Chem.* **50**, 443–485 (1999).
2. M. P. Jacobson and R. W. Field, *J. Phys. Chem.* **104**, 3073–3086 (2000).
3. H. Partridge and D. W. Schwenke, *J. Chem. Phys.* **106**, 4618–4638 (1996).
4. J. M. Bowman, B. Gazby, J. A. Bently, and T. J. Lee, *J. Chem. Phys.* **99**, 308–323 (1993).
5. M. P. Jacobson, C. Jung, H. S. Taylor, and R. W. Field, *J. Chem. Phys.* **111**, 600–618 (1999).

6. Z. M. Li, L. Xiao, and M. E. Kellman, *J. Chem. Phys.* **92**, 2251–2268 (1990).
7. L. Xiao and M. E. Kellman, *J. Chem. Phys.* **93**, 5805–5825 (1990); *J. Chem. Phys.* **93**, 5821 (1990).
8. R. T. Lawton and M. S. Child, *Mol. Phys.* **40**, 773–792 (1980).
9. M. S. Child, in “Computational Molecular Spectroscopy” (P. Jensen and P. R. Bunker, Eds.), Chap. 18. Wiley–Interscience, Chichester, 2000.
10. M. S. Child, “Semiclassical Mechanics with Molecular Applications.” Oxford Univ. Press, Oxford, 1991.
11. M. S. Child and L. Halonen., *Adv. Chem. Phys.* **57**, 1–58 (1984).
12. R. N. Dixon, *Trans. Faraday Soc.* **60**, 1363–1368 (1964).
13. J. W. C. Johns, *Can. J. Phys.* **45**, 2639–2650 (1967).
14. M. S. Child, T. Weston, and J. Tennyson, *J. Mol. Phys.* **96**, 371–379 (1999).
15. M. Quack, *Annu. Rev. Phys. Chem.* **41**, 839–879 (1990).
16. A. J. Lichtenberg and M. A. Lieberman, “Regular and Stochastic Motion.” Springer-Verlag, New York, 1983.
17. T. Poston and I. Stewart, “Catastrophe Theory and Its Applications.” Pitman, London, 1978.
18. H. Goldstein, “Classical Mechanics,” 2nd ed. Addison–Wesley, New York, 1980.
19. M. Lewerenz and M. Quack, *Chem. Phys. Lett.* **123**, 197–202 (1986).
20. D. Noid, M. L. Kosykowski, and R. A. Marcus, *Annu. Rev. Phys. Chem.* **31**, 267–309 (1981).
21. H. S. Taylor and J. Zakrzewski, *Phys. Rev. A* **38**, 3732–3748 (1988).
22. E. Pollak, *Philos. Trans. Roy. Soc. London A* **332**, 343–359 (1990).
23. G. García de Polavieja, N. G. Fulton, and J. Tennyson, *Mol. Phys.* **83**, 361–379 (1994).
24. J. Svitak, Z. M. Li, J. Rose, and M. E. Kellman, *J. Chem. Phys.* **103**, 3870–3870 (1995).
25. C. D. Cooper, Chemistry Pt II thesis. Oxford University, 1999 (unpublished).
26. M. Lewerenz and M. Quack, *J. Chem. Phys.* **88**, 5408–5432 (1988).
27. M. S. Child, *J. Phys. A* **31**, 657–670 (1998).
28. M. P. Jacobson and M. S. Child, *J. Chem. Phys.* **114**, 262–275 (2001).
29. M. Joyeux, S. Yu. G. Schinke, and R. Schinke, *J. Chem. Phys.* **109**, 8342–8354 (1998).
30. L. R. Bates, *J. Appl. Math. Phys.* **42**, 837–847 (1991).
31. R. Cushman, *Centruum Wiskd. Inf. Newslett.* **1**, 4–18 (1983).
32. G. Arfken, “Mathematical Methods for Physicists,” 3rd ed. Academic Press, San Diego, 1985.
33. B. V. Chirikov, *Phys. Rep.* **52**, 263–379 (1979).
34. M. Tabor, “Chaos and Integrability in Non-linear Dynamics.” Wiley–Interscience, New York, 1989.
35. S. C. Farantos, *Int. Rev. Phys. Chem.* **15**, 345–374 (1996).
36. M. E. Kellman, *J. Chem. Phys.* **93**, 6630–6635 (1990).
37. J. E. Baggott, *Mol. Phys.* **65**, 739–749 (1988).
38. Z. Lu and M. E. Kellman, *J. Chem. Phys.* **107**, 1–15 (1997).
39. S. Keshavamurthy and G. S. Ezra, *Chem. Phys. Lett.* **259**, 81–90 (1996).
40. J. Rose and M. E. Kellman, *J. Chem. Phys.* **103**, 7255–7268 (1995).
41. S. Keshavamurthy and G. S. Ezra, *J. Chem. Phys.* **107**, 156–179 (1997).
42. M. P. Jacobson and M. S. Child, *J. Chem. Phys.* **114**, 250–267 (2001).
43. M. P. Jacobson and M. S. Child, *J. Phys. Chem.* **105**, 2834–41 (2001).